Mechanics & Industry **26**, 33 (2025)
© M. Serretiello et al., Published by EDP Sciences 2025
https://doi.org/10.1051/meca/2025026

Mechanics & Industry

Available online at:
www.mechanics-industry.org

Original Article

Open Access

Numerical and experimental modelling of mechanical springs made of lattice material

Mathilde Serretiello, Manuel Paredes, and Eduard Marenic*

Univ Toulouse, IMT Albi, INSA Toulouse, ISAE-SUPAERO, CNRS, ICA, Toulouse, France

Received: 18 April 2025 / Accepted: 6 September 2025

Abstract. Additively manufactured beam-based lattice materials made of repeating unit cells are nowadays used in modern lightweight engineering design. In this paper we propose a redesign of a typical mechanical spring aiming to achieve reduced material usage by introducing a multi-scale architecture. A parametric model of the helical spring made of lattice material is developed to enable both rapid geometry and finite element preparation as well as the optimization based on differential evolution algorithm. Judicious multiscale optimization of the lattice structure together with the stress homogenization based on the lattice gradient, proved to significantly improve the spring stiffness. Experimental validation of the proposed redesign is performed on the additively manufactured spring prototypes.

Keywords: Lattice materials / additive manufacturing / mechanical spring / differential evolution / gradient lattice / multiscale optimization

Acronyms and notation

AM	Additive Manufacturing
FE	Finite element
ht	Coil height
LM	Lattice Materials
n_c	Wire section circumference points
n_r	Wire section radial points
n_s	Sections per coil
r_{beam}	Beam radius
R	Coil radius
r_{in}	Inner wire radius
r_{out}	Outer wire radius
RP	Reference Point
SLM	Selective Laser Melting
SLS	Selective Laser Sintering
UC	Unit Cell

1 Introduction

Achieving further weight reduction in the design of modern engineering products is often based on a straightforward concept: increasing the proportion of voids in the material in a structured and well-planned way. The rapid advancement of Additive Manufacturing (AM) technologies, particularly Selective Laser Melting (SLM) for metals and Selective Laser Sintering (SLS) for polymers, has made it possible to design materials at the micro-scale. This has led to the creation of Lattice Materials (LM), which exhibit strength and stiffness that scale proportionally with the solid volume fraction of the material [1]. LM are on small-scale topologically ordered, three-dimensional open-celled structures composed of repeating Unit Cells (UCs). Nowadays, LM are usually created of beam-based (focus of this work, Fig. 1) or surface-based UCs, however, the number of options and possible realizations is endless. This capability enables the design of lightweight structures that maintain strength and stability making them interesting in different applications (see Figs. 1b, 1c), and in particular in the aerospace industry [4,5]. In addition, LM can be optimized for specific mechanical properties, such as stiffness (or its inverse − compliance), by adjusting the lattice structure. More precisely, the macroscopic elastic and fatigue behavior of these structures depend on different parameters related to: UC topology, material, manufacturing process, and loading conditions.

The choice of these parameters leads to either bending- or stretch-dominated UC's overall mechanical response. Bending-dominated LM absorb a large amount of mechanical energy at lower stresses and are generally characterized by a stress plateau [6] after an initial stress peak. Stretch-dominated LM, on the other hand, respond with the predominant traction/compression of the beams

* e-mail: marenic@insa-toulouse.fr

This is an Open Access article distributed under the terms of the Creative Commons Attribution License (https://creativecommons.org/licenses/by/4.0), which permits unrestricted use, distribution, and reproduction in any medium, provided the original work is properly cited.

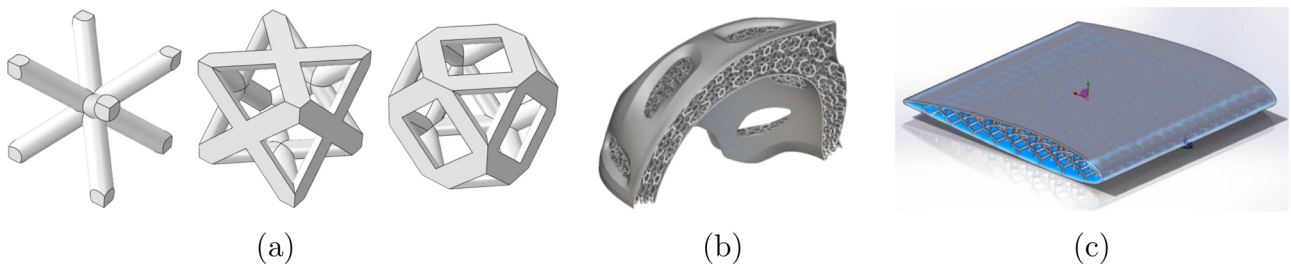

Fig. 1. (a) example of different unit cells (BCC, FCC, CO); (b) example of lattice materials based protective equipment (helmet) [2]; (c) aeroplane wing made of lattice material within the airfoil skin [3].

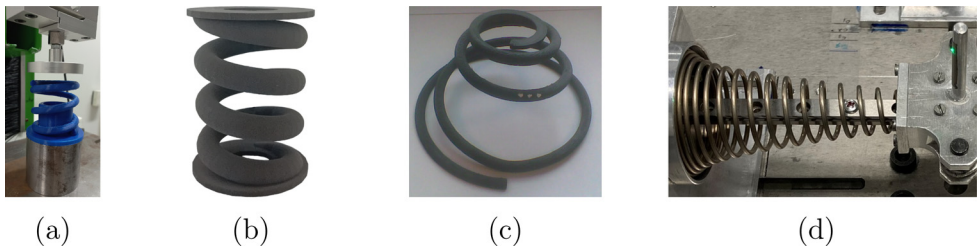

Fig. 2. Additively manufactured springs: (a) with uniform coil diameter made with FFF process and PLA filaments [8], (b) made with sls process and PA powder, (c) non-uniform coil diameter made with FFF and PLA filaments [9]. (d) Non-uniform coil steel spring in NES application [10].

and exhibit higher yield stresses. Thus, these structures are more suited to lightweight and higher stiffness applications. There is a vast literature related to the usage of LM in mechanical energy absorption, see an exhaustive review [7] and references therein. In these works the application is often related to protective systems, (Fig. 1b) and the numerical and experimental investigation is mainly related to compression type of load on the simple prismatic samples built of LM.

In this paper, the focus is on redesigning and optimizing mechanical helical springs (see Fig. 2) by introducing a multiscale architecture. A spring is a mechanical device whose principal role is to store and restore mechanical energy by elastic deformation. Springs come in many shapes and sizes and are used in different mechanisms (e.g. deployable systems of a satellite [11], suspensions systems, etc.). Taking, for instance, a standard helical compression spring, from Figure 2, we notice that the spring action is naturally multiscale. More precisely the spring action is happening on two scales: (i) structural scale – compression which takes the applied force in the suspension mechanism, and (ii) material scale – torsion of the homogeneous cross-section of the wire which stores the mechanical energy. Commonly, the spring is made of the round high-carbon steel wire with uniform coil diameter (conical Figs. 2c and 2d or barrel shapes are sometimes used to meet particular load-deflection requirements). In this sense, traditional manufacturing methods no longer offer the possibility of improvement [5].

In addition to the described multiscale character of springs, two key benefits arise from using AM when designing mechanical springs: the ability to introduce a hierarchical complexity and multiple materials within a single printed spring. The main interest of exploring the first, addition of hierarchical complexity, is to introduce the non-homogeneous, lattice spring section using topologically ordered UCc (as in Fig. 1a). That is, to replace standard homogeneous wire cross-section (material scale (ii) – which is responsible for the storage and restitution of mechanical energy) with the LM. In order to function properly, the mechanical spring is on the scale of the device a carefully designed structure, e.g. the helical or wave shape with different pitch. Interestingly, using AM together with LM which we propose in this work opens the possibility to redesign the spring both on the structural (i) and material scale (ii).

As mentioned and cited above, in the majority of the published work on the crashworthiness and protective equipment application, the role of LM is to favor energy dissipation. In that sense, the experimental modelling is usually related to the compression of simple testing specimens made of LM [12,13]. While there is extensive literature on the compression loading of LM for energy absorption applications, references specifically addressing the modelling of additively manufactured LM-based mechanical springs remain relatively sparse. Saleh et al. [14] study the effect of spring geometry on the shear modulus of Ti-6Al-4V helical springs produced by SLM, showing how smaller pitches influence mechanical performance. In [15] the investigation of the optimization of variable dimension wave springs using experimental methods and finite element (FE) analysis is presented. Introduction of the concept of customizable 3D-printed springs, emphasizing design flexibility is given in [16]. Sacco et al. [5] explore 3D-printed springs for aerospace applications, focusing on performance under extreme conditions.

To our knowledge, none of the references is adding LM to the above mentioned (ii) material scale, for instance in the cross-section of the helical spring. Our goal here is to explore this possibility. Unlike the majority of the literature dealing with LM, which focuses on the energy dissipation and simple compression tests, for the helical mechanical spring the loading regime and dominant loading mode change significantly, namely:

– The absorbed energy is supposed to be fully reversible (elastic) to ensure the spring restitution.
– On top of that, the absorbed energy within a helical spring is principally related to the torsional mode. That is, the stresses on the cross-section of the wire are mainly shear stresses which give rise to the stress resultant in terms of the torsional moment.

Thus, the general tendencies reported in the available literature on the application of LM need to be verified. A preliminary experimental study of torsional properties of additively manufactured LM with the spatial gradient is presented in [17]. Both surface-based (TPMS – triply periodic minimal surfaces) and beam-based LM were designed in cylindrical shape specimens produced with HP Multi Jet Fusion process. Not surprisingly, they conclude that the stiffness and energy absorption can be improved by optimizing material distribution, namely, they alter UC thickness which increases towards the outer surface of the cylindrical specimen.

The main objective of this study is to design, test and validate a compression spring made of LM at the material scale. To this end, the structure of the paper is organized as follows. Section 2 introduces the key features of the parametrized geometrical modelling of the spring coil made of lattice material. With the parametrized model, the choice of optimal unit cell is detailed. Next section deals with the whole lattice spring model. The optimization of the previously chosen unit cell in terms of the stiffness-to-mass ratio is presented together with the possibility of adding a material gradient. Section 4 discusses the modelling, additive manufacturing and post-processing of the compression, helical spring prototypes made of lattice material, including the elementary testing coupons for the material parameters identification. Special attention is given to the particularities of the rather challenging cleaning process in the preparation phase identifying auxiliary and temporary features. Finally, experimental results are discussed and compared with finite element modelling. Last section lists the key conclusions and research perspectives.

2 Designing a helical spring made of lattice material

2.1 Key features of the lattice spring model

The first step in designing a mechanical spring based on LM is to explore the possibility of adding a hierarchical complexity in the cross-section of the spring. In order to pave the way of redesigning the mechanical spring, a common component in mechanical engineering, we start with a well accepted helical shape on the structural level. We shall, thus, explore the possibility of replacing the standard wire design with LM. Initial tests were conducted in a somewhat simplified context, using straight, cylindrical lattice specimens similar as in [17]. The specimens were designed with the Ntop software [18] which has a built-in support to generate the transformed UCs fitting the cylindrical shape. Finally, the specimens were manufactured using the SLS process to evaluate their suitability for the spring design. It turned out that for SLS process, the major obstacle was the post-processing. The removal of unsintered powder trapped inside the lattice proved to be very difficult or even impossible, contrary to the MFJ process presented in [17]. To address this issue, a simple redesign based on a hollow cylindrical sample was made.

Following the conclusions and the experience from the initial tests performed on the straight, cylindrical lattice samples, the coil wire sections were designed as hollow. The geometry of the spring is first discretized into a structured hexahedral layout composed of brick-shaped cells, which later serve as containers for inserting lattice UCs. This structured grid provides a flexible framework for parametrically generating various lattice spring configurations with controlled material distribution. To that end, we introduce two sets of parameters: geometrical and discretization. Geometrical parameters define the shape and size of the spring: r_{in} and r_{out} is inner and outer radius of the wire cross-section, r_{coil} is the coil radius, and ht is the vertical pitch of the spring (all depicted in blue in Fig. 3). Discretization parameters in our context defines how finely the geometry is sampled with: n_c and n_r being the number of divisions in circumferential and radial directions of the wire cross-section (Fig. 3a) while n_s represents the number of divisions per coil (Fig. 3b). Having these parameters in hands, the hexahedral cells are defined using a parametric mapping based on the following coordinates: (1) r and θ being the polar coordinates in the wire cross-section (Fig. 3a); (2) ϕ being angular coordinate along the helical spring centerline (coil progression shown in Fig. 3b); (3) h representing a vertical elevation ($y-$direction) between cross-sections along the helix (Fig. 3c). These coordinates define a smooth helical path, and the corresponding local reference frames provide a basis for orienting and positioning UCs within the spring volume. The set of all (r, θ, ϕ, h) positions forms a structured hexahedral grid to be populated with a lattice UC. The entire spring geometry is then constructed by iterating over discrete index increments i, j, and k corresponding to circumferential, radial, and axial directions, respectively, as detailed in the parametric equations in sequel. For the development of the parametric equations defining the spring geometry, we introduce three discrete index increments in the range:

$$i\in\{0,1,\ldots,n_c-1\}, j\in\{0,1,\ldots,n_r-1\}, k\in\{0,1,\ldots,n_s-1\}.$$

Using these indices, the point locations are defined as follows:

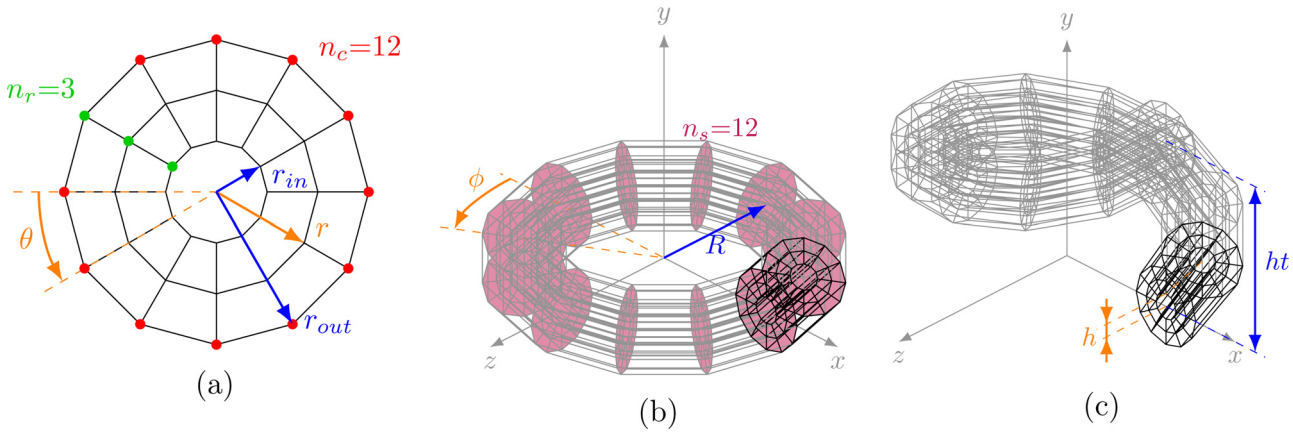

Fig. 3. Illustration of the parametric mapping used to generate the spring geometry. (a) Unit cells are distributed in a polar grid within the circular cross-section using coordinates (r, θ). (b) This cross-section is swept along a circular coil path, introducing the circumferential coordinate ϕ. (c) The full helical spring is formed by stacking multiple coils vertically, using the elevation coordinate h. This multi-stage mapping allows a Cartesian unit cell grid to be morphed onto a smooth helical spring with a curved lattice structure.

– Within the cross-section, in polar coordinates (r, θ) (Fig. 3a)

$$\theta_i = \frac{2\pi}{n_c} i \tag{1}$$

$$r_j = r_{\text{in}} + \frac{(r_{\text{out}} - r_{\text{in}})}{n_r - 1} j. \tag{2}$$

– Along the helical coil path, using the angular progression ϕ (Fig. 3b)

$$\phi_k = \frac{2\pi}{n_s} k. \tag{3}$$

– In the vertical (axial) direction, where h_k is the vertical elevation increment per unit cell (Fig. 3c)

$$h_k = \frac{h_t}{n_s} k. \tag{4}$$

Given these parameters, the Cartesian coordinates (x, y, z) of each lattice node along the spring can be calculated using the following parametric equations:

$$\begin{aligned} x &= \big(R + r_j \cos(\theta_i)\big) \cos(\phi_k), \\ y &= r_j \sin(\theta_i) + h_k \sin(\phi_k), \\ z &= \big(R + r_j \cos(\theta_i)\big) \sin(\phi_k). \end{aligned} \tag{5}$$

It is important to note that in conventional spring designs, the circular cross-section of the wire is normal to the helical centerline. In our model, by contrast, the cross-sections are aligned with the vertical (y) direction for the purpose of defining a structured hexahedral grid. Since the goal of this study is to explore novel spring designs based on LM, this deviation from classical alignment is not restrictive. In fact, when observed in the plane normal to the helical centerline, our cross-section becomes slightly elliptical. For the helix angle used in this work (9°, a typical value for standard coil springs), the geometric distortion introduced by this alignment is minor, and represents a maximum diameter reduction of approximately 1.2% in one direction. This confirms that the geometric deviation remains negligible, and the comparison to conventional cylindrical wire springs remains valid.

With these parametric equations, a Python script was developed to automate the generation of both CAD and finite element models. The finite element modeling process was integrated into the Abaqus Scripting Interface, enabling quick creation and analysis of lattice spring geometries. This scripting approach allows for systematic testing of various lattice architectures to identify the most efficient configurations for the target application. The performance of single coils filled with 12 different UCs types is compared under compression in Section 2.2.

2.2 Preliminary numerical analysis: choosing the optimal UC candidate

Finite element simulations were conducted using Abaqus software to evaluate the efficiency of a coil spring made of 12 different unit cells (see Fig. 4). Efficiency refers to the spring's ability to store mechanical energy when loaded in compression. It can also be associated with the area under the force-displacement curve, which follows a linear trend with a slope equal to the spring stiffness. Therefore, for the weight reduction in the design of engineering products based on LM, and for the imposed displacement tests, the analysis focuses on the mass-specific stiffness k_m as a key parameter to assess spring performance.

For the preliminary numerical analysis, the coils were characterized by the following geometric parameters: (i) $R = 32$ mm, $r_{\text{out}} = 8$ mm, $r_{\text{in}} = 4$ mm, and $n_r = 2$ were fixed; while (ii) n_c and n_s were varied, to try numerous lattice refinements (Fig. 6a spring made of the Cuboctahedron (CO) UC comprises 279 elements/coil as a product of $n_c = 9$ and $n_s = 31$).

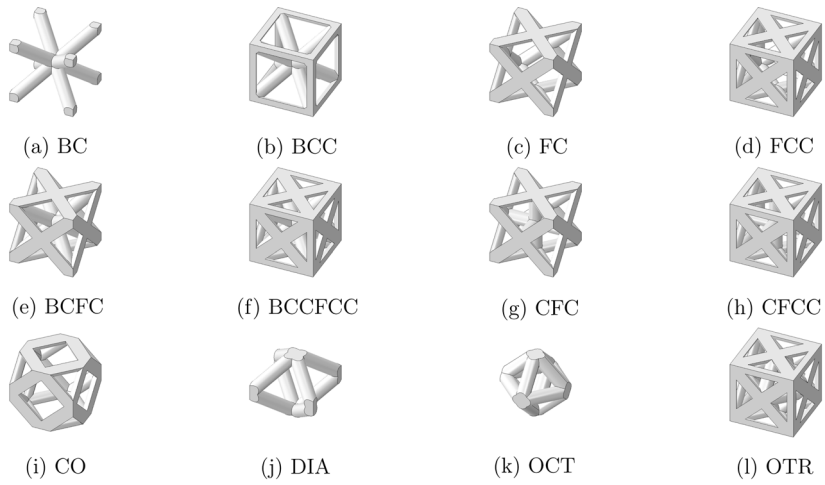

Fig. 4. An overview of the 12 different UC tested in finite element analysis. The UCs abbreviations used in sequel are: Body Center (BC), Body-Centered Cubic (BCC), Face Center (FC), Face-Centered Cubic (FCC), Body Face Center (BCFC), Body Face-Centered Cubic (BCCFCC), Center Face Center (CFC), Center Face-Centered Cubic (CFCC), Cuboctahedron (CO), Diamond (DIA), Octahedron (OCT), Octet-Truss (OTR).

Finite element model is created as a wire structure dicretized with shear flexible, linear interpolation beams (type B31) with 6 degrees of freedom. On top of the fixed geometric parameters (i) presented above and on Figure 3, for the beam FE model, we ought to define the beam section properties. The latter was modeled as circular with $r_{\text{beam}} = 0.65$ mm. The cross-sections on the extremities of the coil were used to impose the displacement boundary conditions. The lower section was coupled (Kinematic coupling) to a fixed Reference Point (RP) located along the central axis of the spring to impose clamped boundary conditions, while the upper section was coupled to another RP, also positioned on the spring's axis, to which a vertical displacement $u_y = -10$ mm was applied. The degrees of freedom of displacement u_x and u_z were left free. In addition, to ensure a controlled loading path, the rotational degrees of freedom were constrained such that $\theta_x = 0$, and $\theta_z = 0$. Upon completion of each of total of 350 simulations, the vertical reaction force (F_R) and the approximated total mass (m) of the model were recorded. The total mass m recorded from FE model is said to be 'approximate' since the beam FE model doesn't take into account the overlap of the beams in the lattice nodes. From these results, firstly spring stiffness (k) and then the mass-specific stiffness k_m was calculated for each UC. Related to the approximate mass estimate, as a comparison a full cylindrical wire made with the same material would induce a mass of about 0.04 kg (with a stiffness of 13000 N/m, and a mass-specific stiffness of about 324 N/mm/kg). As can be seen from Figure 5b some UCs lead to similar or even higher mass (which is theoretically impossible). Exact computation of the mass of the lattice spring containing numerous voids would lead to a greater value of the mass-specific stiffness than the bulk helix wire. Figure 5 presents selected results from the preliminary numerical study, comprising 350 simulations of 12 UCs with varying refinement levels. The evolution of (a) spring stiffness (k), (b) approximate total mass (m), and (c) mass-specific stiffness (k_m) is shown for fixed $n_c = 9$. As expected, stiffness increases with refinement but tends to plateau, while approximate mass grows nearly proportionally with n_s. This trade-off results in a peak in k_m, identifying an optimal refinement around $n_s = 37$. Among all candidates, the CO unit cell consistently exhibits the highest k_m across the full refinement range $15 \leq n_s \leq 47$ and $7 \leq n_c \leq 14$ (the latter not fully shown for clarity), making it the most promising candidate for further optimization.

The performance of certain UC in terms of k_m is directly related to the stress distribution within the lattice structure. To that end, we give in Figures 6a and 6b the distribution of the normal stresses in each beam (σ'_{xx}) of the lattice structure of the single spring coil, for the best (CO) and one of the worst (BCC) performing UC. Note that σ'_{xx} is given in the local beam coordinate system, where x' is the axis of each beam in LM. It can be seen from Figures 6a and 6b mostly in the region in the vicinity of the inner coil diameter (r_{in} in Fig. 3a), that the beams of each UC are asymmetrically loaded in tension (red) and compression (blue). As mentioned in Introduction, this phenomenon reflects the torsion of the coil which can, in the limiting case of pure shear, be represented with the opposite tension/compression principal (normal) stresses orientated towards principal vectors, that is, ±45° relative to the helicoidal neutral fiber of the coil. Similarly to a conventional spring [19], higher stresses and strains are observed in the region in the vicinity of the inner coil diameter. As might be expected, when this tension-compression interaction is more pronounced, which occurs typically when the beams are oriented near 45° relative to the neutral fiber of the spring, the spring stiffness increases. Finally, from the preliminary numerical analysis, based on the performance in terms of k_m, we choose CO UC as the optimal candidate for the following optimization. The other UCs (especially those with significantly lower k_m values, as BCC UC), were not considered relevant.

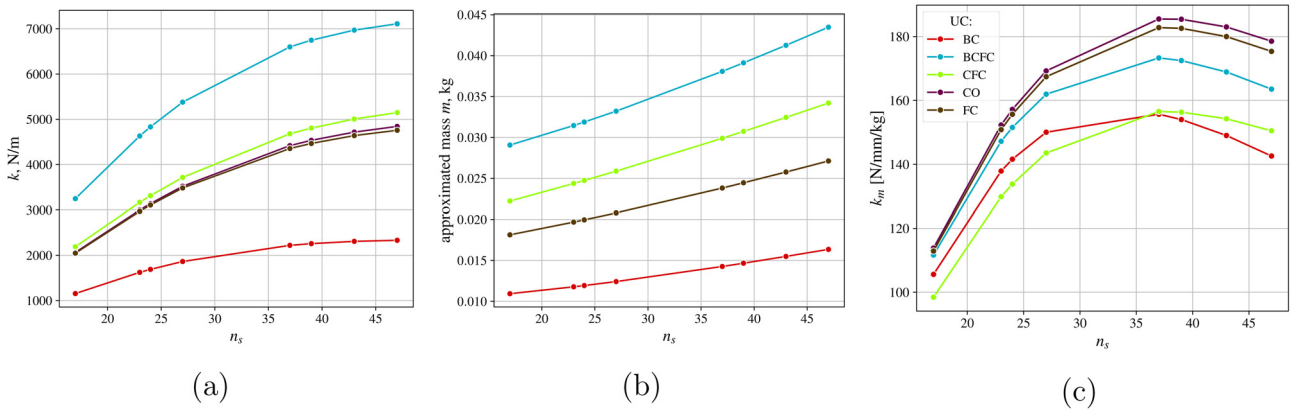

Fig. 5. Preliminary analysis of the effect of lattice refinement (n_s) on (a) spring stiffness (k), (b) approximate mass (m), and (c) mass-specific stiffness (k_m), for 5 different UCs at fixed refinement in circular direction ($n_c = 9$).

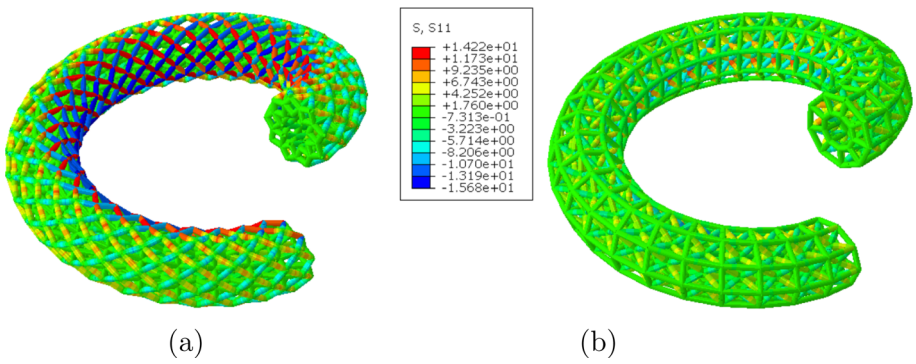

Fig. 6. Beam FE model and the distribution of stress σ'_{xx} (MPa) in a single spring coil made of (a) CO and (b) BCC UC. The stress is plotted on the model with $ht = 32$ mm, $R = 32$ mm, $r_{in} = 4.0$ mm, $r_{out} = 8.0$ mm, $n_r = 2$, $n_s = 31$, $n_c = 9$, $r_{beam} = 0.65$ mm.

3 Lattice spring modelling and optimization

3.1 Modelling of the whole LM spring

Following the preliminary analysis performed on the single coil in order to choose the optimal UC, we turn now to the development of the spring prototype. Following the previously explained design process of the coil, the python script was used to generate both the FE and CAD models of the whole helical spring made of LM. The coils-end geometry can have a significant influence on a spring behavior [20]. Thus, in addition to the automated model creation, two bulk circular end-plates were added on the top and on the bottom of the CAD model of the spring lattice structure, see Figure 7a. Analogously as for the single coil, FE model is created as a wire structure dicretized with beam FEs to which a circular cross-section is assigned. To facilitate the comparison, two cutting planes intersect the beams to model the bulk-end plates, which are in FE model considered as rigid[1]. More precisely, the endpoints of the beams lying within each cutting plane are coupled to a reference point positioned on the same plane and aligned with the spring's $y-$axis, as depicted in Figure 7b with yellow lines. Imposed boundary conditions are similar to the single coil simulations: The reference point located at the bottom of the spring, is clamped, while the reference point at the top of the spring, is assigned a displacement U along the y-axis. Likewise, the rotations about x- and z-axes are restrained to align the model to the the kinematics of the bulk end-plates as much as possible, while the displacements u_x and u_z are left free.

3.2 Optimization

To reduce the number of printed and tested samples required to identify the most efficient spring design, the whole spring model detailed above will be coupled with an optimization algorithm. This algorithm maintained the same outer dimensions and wire section radial points (n_r), while adjusting parameters related to the number and size of cells. Specifically, it varied the wire section circumference points (n_c), the sections per coil (n_s), the beam radius (r_{beam}), and the inner wire radius (r_{in}), while $n_r = 2$.

Thus, the four design variables ($N = 4$), that define the lattice-based spring geometry, involved: (1) Discrete integer variables n_c, $n_s \in \mathbb{Z}$ (in the range reported above); (2) Continuous variables $r_{beam} \in \mathbb{R}_{\geq 0.5\text{mm}}$ and $r_{in} \in \mathbb{R}_{\geq 4\text{mm}}$,

[1] Given the difference in stiffness between bulk end-plate and slender beams in LM, modelling the end plates as rigid is reasonable choice.

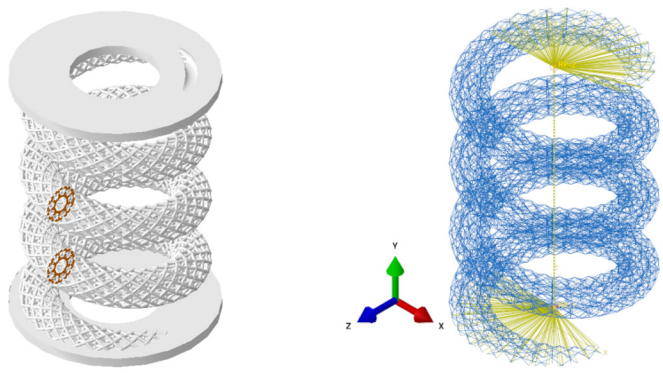

(a) (b)

Fig. 7. CAD (a) and beam FE (b) models of the whole spring with LM made of CO UCs. The bulk end-plates are added to lattice structure in CAD model. Corresponding coupling for the application of the boundary conditions is created in FE model.

that are conveniently arranged in parameter vector $\mathbf{p} = [n_c,\ n_s,\ r_{beam},\ r_{in}]$. We note that the lower limits of r_{beam} and r_{in} are aligned with the manufacturing constraints (choice of the process and material) as detailed in the following section. As it was the case for preliminary analysis, the objective was to maximize the stiffness-to-mass ratio (k_m). To reformulate this as a minimization problem, the objective function was defined as the inverse of this ratio

$$J(\mathbf{p}) = \frac{1}{k_m}, \quad \text{with} \quad k_m(\mathbf{p}) = \frac{F_R(\mathbf{p})}{m(\mathbf{p}) \cdot u_y}, \tag{6}$$

where the reactive force F_R and approximate mass m of the spring are extracted from FE simulation, while u_y denotes the imposed vertical displacement applied to the top of the spring. In addition, a constraint was introduced to ensure that springs whose cell spans would overlap, thereby eliminating the voids in the lattice structure, were excluded from the optimization process. More precisely, the relative volume (V_r) of the UC, that is, the fraction of the UC's volume occupied by material, has to be limited with the threshold V_{max}:

$$V_r(\mathbf{p}) = \frac{V_{solid}(\mathbf{p})}{V_{cell}} \leq V_{max}, \tag{7}$$

Thus, the optimisation problem can be formally given as

$$\min_{\mathbf{p}} J(\mathbf{p}) \quad \text{subject to} \quad V_r(\mathbf{p}) \leq V_{\max}. \tag{8}$$

Here, $\mathbf{p}$ denotes the vector of optimization variables, including n_c, n_s, r_{beam}, and r_{in}, as introduced in Section 2.1.

The optimization process was implemented using the `differential_evolution` function from the scipy. optimize library [21]. A differential evolution algorithm was chosen for its ability to efficiently explore large parameter space and is well-suited when optimizing complex, mixed variables non-linear objective functions (Fig. 5c depicts the non-linear relation $k_m(n_s)$). At each iteration, (i) the variables were adjusted, (ii) a FE model was regenerated with the script presented above, and (iii) another Abaqus simulation run was executed. At the end of these three steps of each iteration, the applied force and mass are recorded to compute the mass-specific stiffness of the spring. This process was repeated in a loop until convergence was achieved, resulting in the optimal spring configuration. The algorithm was executed with a population size[2] of 10, a maximum of 10 iterations[3]. Additionnaly, 4 bounds (N=4) were taken to constrain the variables within specified minimum and maximum values : $9 \leq n_c \leq 14$, $46 \leq n_s \leq 74$, $0.5 \leq r_{beam} \leq 0.8$ and $4.0 \leq r_{in} \leq 6.0$. This configuration resulted in a maximum of 440 function evaluations. We note also that in order to verify the constraint (7), in practice, we took the threshold that implies that the UC is almost fully occupied by material (and merits to be discarded from the optimization process) as $V_{max} \leq 0.9$. That is, the optimization problem is classified as unconstrained, and unacceptable configurations $V_{max} > 0.9$ were discarded manually in the step (ii) after the generation of FE model.

Figure 8 presents the results of the optimization. It displays the values of the objective function and the local minima identified every 40 evaluations (population size $\times N$) corresponding to each iteration, see Figure 8 (left). By focusing on the local minima, Figure 8 (right), the minimization procedure can be traced as the values of the objective function value decreases and converges towards an estimated global minimum. The optimization process terminates when the relative difference between the best and worst objective function values in the population drops below the given tolerance, taken here as 0.01. This condition ensures that further iterations do not yield a significant improvement in the objective function, and indicates the population convergence. In our example, convergence is visible from the plot of the best objective function value against both the number of function evaluations and iterations, which shows diminishing improvements while approaching towards the global minimum. For the CO spring with $ht = 32$ mm, $r_{coil} = 32$ mm, $r_{out} = 8.0$ mm, $n_r = 2$, we end-up with $n_s = 58$, $n_c = 13$, $r_{beam} = 0.72$ mm, $r_{in} = 5.99$ mm.

3.3 Adding lattice gradient for the stress homogenization

As discussed previously (and depicted in Fig. 6), springs experience significantly higher stress at the inner coil fiber and lower stress at the outer coil fiber. When designing springs for additive manufacturing using lattice materials (LM), it is natural to attempt to homogenize the stress distribution over the entire wire cross-section using so called functionally graded lattice structures. The 'grading' can generally be achieved in two ways: by varying the unit cell size, or by modifying the dimensions (the radius) of the beams. Both techniques have been widely studied for controlling relative density and tailoring mechanical response [22,23]. In this work, we adopted the latter

[2] A number of candidate solutions evaluated in each iteration.
[3] This limit was chosen given the cost of finite element simulations.

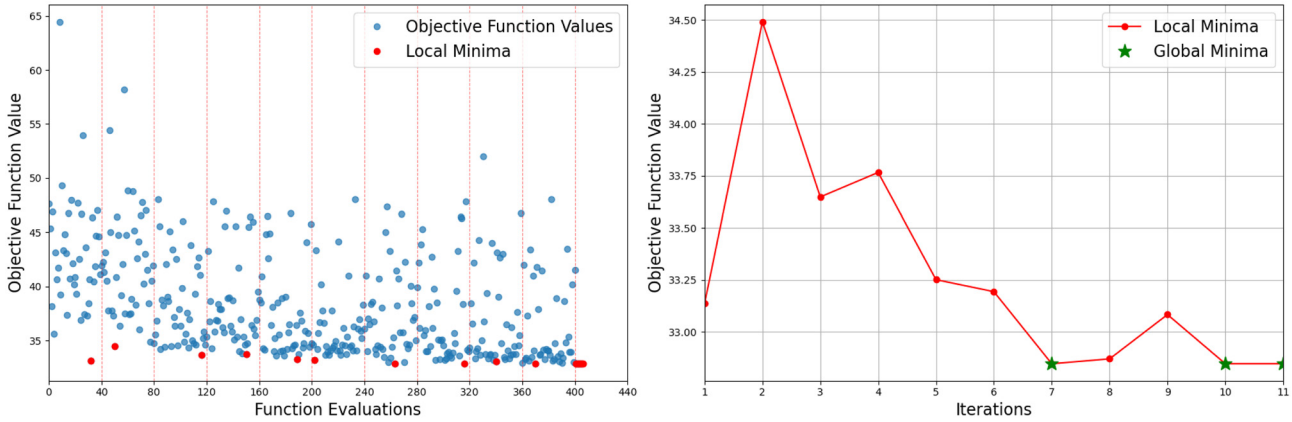

Fig. 8. Results of the topological optimization showing the objective function values and local minima. In the left subplot all the evaluations are presented (blue) together with the local minimum (red) for each iteration. The iteration comprising 40 evaluations are separated with vertical grid lines. In the right subplot, the zoom showing only the local minima of objective function (6) vs the optimization iterations is shown.

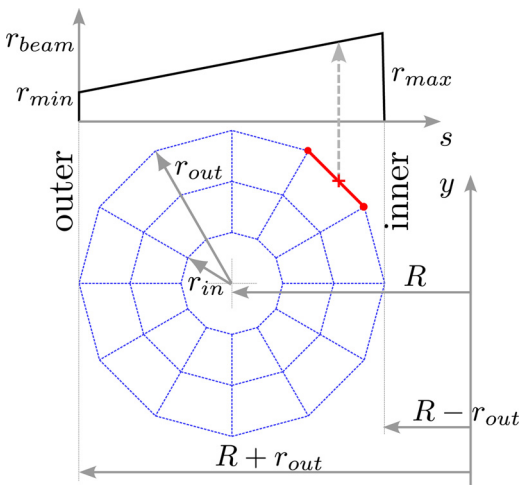

Fig. 9. Gradient beam radius profile $r_{\text{beam}}(s)$ along the radial coordinate s of the spring cross-section. The outer coil fiber corresponds to $s = R + r_{\text{out}}$, and the inner coil fiber to $s = R - r_{\text{out}}$. The beam radius increases linearly from r_{min} to $r_{\text{max}} = f \cdot r_{\text{min}}$ to redistribute material toward higher stress regions. The red beam illustrates how the radius is assigned based on its midpoint position along s: the beam's endpoints are marked with red circles and the midpoint with a red plus symbol.

approach. More precisely our *gradient lattice* aims to assign a larger radius to the beams located near the inner coil fiber, compared to those near the outer coil fiber, thereby increasing material density in regions of higher stress and improving structural efficiency. We note that this can be considered a form of horizontal grading as classified in [23]. The decision to vary the beam radius rather than the size of the unit cells was guided by both modeling and implementation considerations. Since our FE model is based on beam elements, modifying cross-sectional properties allows for straightforward parameterization without requiring re-meshing or altering cell topology. On top of that, this approach preserves connectivity and periodicity, and integrates naturally into our parametric CAD and FE workflows.

Figure 9 illustrates the beam radius variation. A cross-sectional profile of the spring wire is shown, with the horizontal axis corresponding to the radial direction of the coil in the cylindrical coordinate system. The coordinate s spans from the outer surface of the spring ($s = R + r_{out}$) to the inner surface ($s = R - r_{out}$), where R is the spring coil radius. The beam radius increases linearly from r_{min} to r_{max} over this interval. Recall that the cross-section boundaries (inner and outer wire surfaces) are defined by $r = r_{in}$ and $r = r_{out}$. In practice, each beam is assigned a constant radius based on the position of its midpoint along the s-coordinate. This is illustrated in Figure 9, where a representative beam is shown in red, with circular markers indicating its endpoints and a plus symbol marking its midpoint. The value of r_{beam} for that beam is taken from the gradient profile at the midpoint ('+' marker) location.

The spring obtained from the previous topology optimization (with a constant beam radius) was therefore modified to include this gradient definition. For the initial analysis, $r_{\text{min}} = 0.5$ mm was selected based on the manufacturing process and material limitations. Through a series of FE simulations, the optimal scaling factor was found to be $f = 1.6$, resulting in a significantly more uniform stress distribution across the spring wire.

The contour plot of the equivalent (Von Mises) stress for both configurations is depicted in Figure 10 and qualitatively illustrates the effect of stress homogenization. Namely, the localized stress concentrations near the inner coil fiber are reduced when a gradient LM is used. We note that, in the beam FE model used here, the visualization provides only a volumetric impression of the lattice geometry (rendered using Abaqus' "render beam profile" option), rather than a true volumetric or continuum stress field.

4 Lattice spring prototypes, experimental modelling and validation

In order to validate the optimization procedure discussed above, an experimental modelling was performed on the

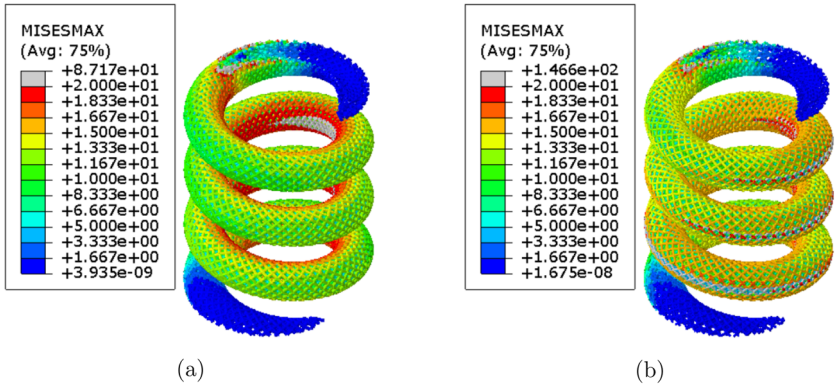

Fig. 10. Beam FE model and the distribution of equivalent stress (MPa) in the (a) previously optimized spring (CO UC) and (b) the same spring with gradient lattice to achieve stress homogenization in the wire cross-section.

lattice spring prototypes. These prototypes were based on the script generated CAD model, see Figure 7a.

4.1 Samples manufacturing and preparation

Generally, the 3D printing of LM made of repetitive UCs (Fig. 4) is challenging, as supports are often required to fill voids and stabilize overhangs even with the surrounding powder in the powder bed fusion processes. In this work the samples were manufactured using Selective Laser Sintering SLS process, specifically with Fuse 1 machine (Formlabs Inc., Somerville, MA, USA) and PA-12 powder material. Key advantage (and motivation) of this choice of process and powder material is that it allowed the lattice spring prototypes (with complex lattice material in helicoidal overall shape) manufacturing without any support. Major disadvantages related to our choice of process and material are:

- The mechanical properties of printed parts are depending on the printing orientation as well as the type of mechanical tests performed, as highlighted in [24] for PA-12 material. However, our helicoidal lattice material springs are composed of a number of beams which are oriented in, virtually, all directions with respect to the printing direction. Thus, as the first choice when modelling our springs, the mean material properties are taken and assigned to each beam in LM.
- The other difficulty is related to cleaning of the residual and unsintered powder. This process, illustrated on Figure 11, starts after the samples were printed, by transferring the chamber to Formlabs Fuse Sift machine[4]. Once most of the unsintered powder was sifted, the parts were initially cleaned as thoroughly as possible using brushes. Final cleaning step was performed by sandblasting with low-pressure (approximately 4 bars) alumina powder, see Figures 11b and 11c.

To simplify this rather laborious powder cleaning process, and avoid damaging the manufactured lattice spring prototype, two features were added in CAD model of the spring:

- We created auxiliary holes in the end-plates to carefully clean the transitional region near the ends, where the LM joins the bulk circular plate to avoid altering the spring behavior;
- A temporary central column along the spring axis was added to reinforce the structure during cleaning (see Fig. 12).

4.2 Control of the lattice spring prototypes

X-ray computed tomography (CT) was performed on the spring prototypes to assess the quality of the manufacturing/cleaning process and to measure the dimensions of the various beams in the lattice structure. Figure 13 presents a typical coil cross-section cutting the beams in our LM. Note that in Figure 13a a CT slice image of the manufactured LM spring is presented (so called 'as-manufactured' configuration [13]), whereas in Figure 13b a typical cross-section of the CAD model of the spring is presented, related to so-called 'as-designed' configuration. There are two key observations from this analysis:

- We note that the image of the 'as-manufactured' configuration shows two distinct material morphologies/densities. The white regions represent fully sintered powder, while the gray regions indicate unsintered or partially sintered powder that was insufficiently cleaned and which is situated in the less accessible regions (for the reference of the position of the cross-sections refer to Figure 7a).
- Moreover, it was observed that the overall dimensions of the beams composing the lattice structure were systematically smaller than in the 'as-designed' configuration. Not surprisingly, decrease of the beam's radius is caused by the cleaning process detailed above, and especially due to the sandblasting process. Our lattice structure made of a number of slender beams is particularly sensitive to the dimensional discrepancy since each beam is covered with the 'skin' of loosely attached or partially sintered powder prone to detachment during cleaning (related to first observation), as noted in [25].

In this paper we seek to characterize the lattice spring on the scale of engineering components. No special treatment was proposed to include mentioned distinct material morphologies or any other defects related to the manufacturing process in our modelling (see [26] for an interesting approach capable of altering beam based lattice

[4] This machine functions as a residual powder recovery station, which is used to sift the unsintered powder as well as to recover, store, and mix the powder for future reuse.

(a) After brushing (b) During sand-blasting (c) End of cleaning process

Fig. 11. Lattice spring prototype cleaning process, plots (a), (b) and (c).

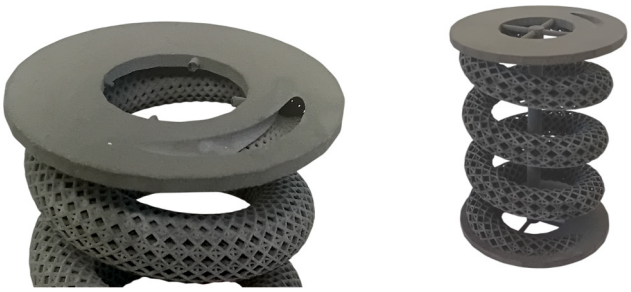

(a) Hole in the end-plate. (b) Temporary central column.

Fig. 12. Specific design to ease the powder cleaning process and to avoid damaging the spring prototype when it carries the weight of non-sintered powder is related to two temporary features: (a) holes are added to spring end-plates, and (b) a central column.

FE model to represent 'as-manufactured' configuration in statistically more reliable way). Complementary microscopic analyses such as SEM could provide further insight into surface morphology, sintering quality, and porosity. These aspects were not included in the present study but will be explored in future work aimed at correlating manufacturing-induced defects with mechanical performance of LM springs. The beam radius reduction due to the preparation/cleaning process will be taken in the average sense. To include the reduction in a qualitative way, various measurements were taken from CT images and using calipers on LM springs made of beams of different dimensions r_{beam}. These measurements were performed on printed spring samples with beam sizes ranging $r_{\text{beam}} = \{0.50, 0.55, 0.65, 0.75\}$ mm and revealed a consistent loss in radius ranging from 0.15 to 0.2 mm. On average the beam radius reduction is significant and is about 25%.

4.3 Lattice spring prototypes

Material parameter identification To determine the mechanical properties of the material, specifically Young's modulus (E)[5], several standard traction tests were performed. To that end, we printed standard test coupons (following the norm ASTM D638 Type 1) which are positioned in different directions with respect to the printing direction, Figure 14a. The values of identified Young's modulus and its variation is given in the table, Figure 14b. For the numerical modelling of the springs with LM in helicoidal structure where the beams are occupying different directions in space, a simple mean of $E = 1090$ MPa is chosen for FE modelling.

Testing spring prototypes Afterwards, printed and prepared spring prototypes were tested in compression using the Andilog Springtest 1 (Andilog Technologies, Vitrolles, France) testing bench, Figure 14c. The spring was positioned vertically on the lower end-plate, and a displacement was applied to its upper end-plate. The compression process was carried out manually in incremental steps of 1 mm, with both the applied displacement and the corresponding force recorded at each step. Testing was terminated either when the machine's force limit of 250 N was reached or when the spring coils came into contact. We report here the results for two lattice spring samples: 1. without topological optimization, and 2. optimized lattice spring. The former consisted of $n_s = 31$, $n_c = 9$, $r_{beam} = 0.65$ mm, while the later consisted of $n_s = 58$, $n_c = 13$, $r_{beam} = 0.72$ mm. The results of these mechanical tests in terms of measured force (F) and imposed displacement (U) are presented with circular markers in Figure 15 for both samples.

Results discussion. From the experimental results we can note that the springs behave linearly below about 20 mm of the spring compression (U). Linear regression curves were added on this linear part of the experimental curves to determine the stiffness of the springs. The stiffness identified from the force-displacement data in the first sample was $k = 534.1$ N/m, while the sample 2 gives $k = 1505.4$ N/m. We note that our optimization presented in Section 2 resulted in almost 300% gain in stiffness of the lattice spring prototype.

In order to establish a meaningful basis for comparison with previous work [17], an equivalent shear modulus (G_{equ}) was computed for both the cylindrical specimens reported in [17] and the helical lattice-spring developed in the present study. For the cylindrical lattice specimens of the radius $r = 12.5$ mm and a length of $L = 100$ mm,

[5] Given that FE modelling is based on the beam FEs, and that we are interested in linear elastic behavior, Poisson's ratio (ν) is not important.

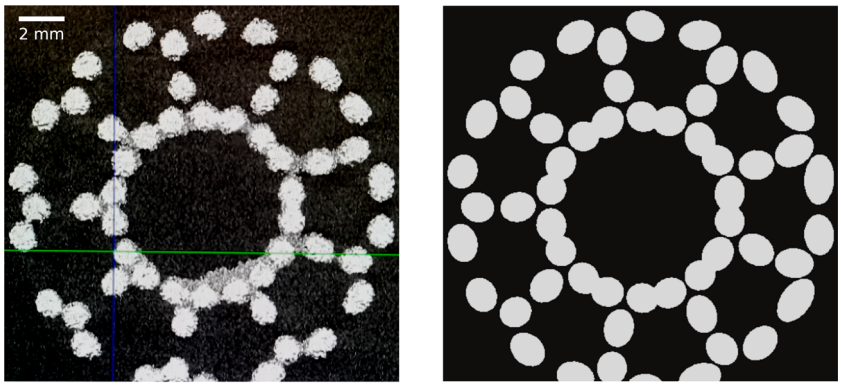

(a) (b)

Fig. 13. Typical spring cross-section cutting the beams in: (a) 'as-manufactured' configuration with the CT slice image; (b)'as-designed' configuration related to CAD model (see Fig. 7a for the reference of the position of the cross-sections).

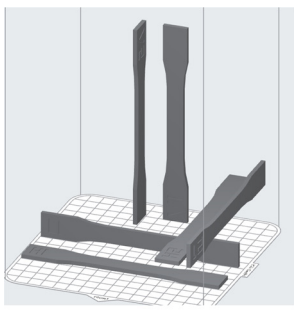

Coupon	E (MPa)
V1	1028
V2	1010
L1	1038
L2	1092
H1	1165
H2	1189

(a) (b) (c)

Fig. 14. (a) Manufactured standard test coupons (following ASTM D638 Type 1) positioned in printing direction (V) and perpendicular to printing direction (L, H); (b) Results of the identified Young's modulus; (c) Testing of the spring prototypes.

G_{eqv} was determined from the torsional stiffness k_t using the relation $G_{eqv,c}$ (9.1).

$$G_{eqv,c} = \frac{32k_tL}{\pi(2r)^4} \qquad G_{eqv,h} = \frac{8kn(2R)^3}{(2r_{out})^4}. \tag{9}$$

Likewise, the equivalent shear modulus ($G_{eqv,h}$) for the helical spring was computed, see (9.2), where k represents the measured stiffness of the spring and n the number of coils R the coil radius, and r_{out} the radius of the spring wire. As we noted in the Introduction, different unit cells were varied and tested in [17]. Taking for instance the beam-based Vertically Inclined structure (called structure VI in [17]), this yields an equivalent shear modulus of $G_{eqv,c} = 33.13$ MPa. Using the equivalent shear modulus as the common basis, $G_{eqv,h}$ was found to be 51.27 MPa for the non-optimized design and 144.52 MPa for the optimized spring configuration. Clearly, we compare here different geometries, unit cells and processes with the same material (PA-12). However, these results indicate that the optimized lattice-based spring exhibits a notably higher equivalent shear modulus, which translates into enhanced load-bearing performance relative to the structures investigated in [17]. The improved performance not only underscores the potential of multi-scale optimization in the design of lattice-based mechanical springs but also provides clear, quantitative design guidelines for achieving superior stiffness-to-mass ratios in practical applications.

A slight nonlinear response was observed in the experimental force−displacement curves for displacements exceeding approximately 20 mm. This behavior is not captured by the present beam-based linear FE model and is not the focus of this study, which targets stiffness optimization in the elastic regime. The observed nonlinearity is believed to result from a combination of geometric and material nonlinearities. Namely, large beam deflections and local plasticity or micro-damage in partially sintered regions, particularly at beam junctions. Since such effects cannot be accurately captured with linear beam elements, they are left for future studies aimed at modeling large deformation and energy-dissipating behavior of lattice springs.

Following the observed trend of the reduction in the beam radius due to the cleaning process, we proceeded with FE modelling (taking the previously identified mean material parameters for PA-12, namely $E = 1090$ MPa and Poisson's ratio $\nu = 0.4$) to adjust the mean beam radius value. This was done in an iterative manner until the model's stiffness matched that of the corresponding experiment. This resulted in an estimated average beam

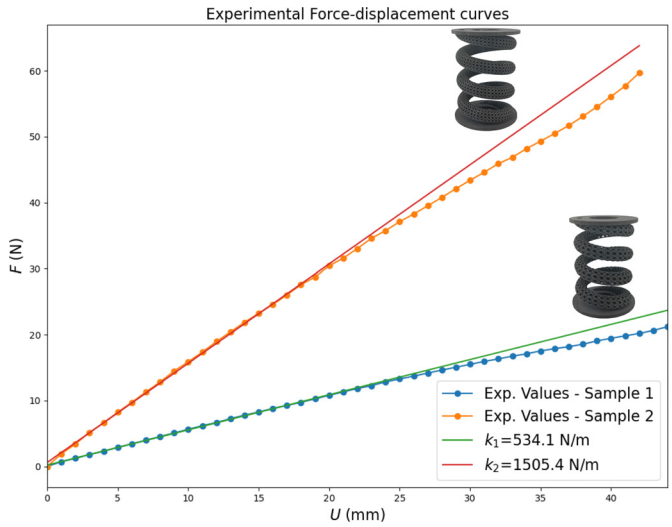

Fig. 15. Experimental force-displacement curves for the two samples.

radius reduction of: (sample 1) from $r_{beam} = 0.65$ mm to $r_{beam,adjust.} = 0.52$ mm (20%); and (sample 2) from $r_{beam} = 0.72$ mm to $r_{beam,adjust.} = 0.55$ mm (24%). These reductions are agreeing well with the trends of the measured reductions reported above.

This modeling approach effectively relates the experimental results and the simulation to identify an equivalent beam radius that explains the observed stiffness. The resulting adjusted radii were consistent with CT-based dimensional measurements, confirming the estimated beam reduction due to cleaning. While this identification strategy proved useful, the FE model remains based on the ideal geometry (with mean radius reduction). Incorporating full "as-manufactured" geometry from CT scans could further improve prediction accuracy by capturing localized deviations and structural imperfections. This remains an important direction for future work, in particular for fatigue applications.

5 Conclusion

In this paper we are dealing with so-called lattice materials made of repeating unit cells. Using these materials in a modern engineering design (in particular in aerospace application) is a promising avenue for weight (and material usage) reduction. To that end, the focus of the presented work is on redesigning and optimizing mechanical helical springs made of (beam-based) lattice materials by introducing a multiscale architecture. More precisely, we seek to replace traditional wire cross-section (called the material scale) with the lattice structure, which results in significant improvement in stiffness-to-mass ratio, up to 300% gain.

Workflow for practical spring design. The fully automated script that generates both CAD and FE models facilitates rapid iteration and optimization, providing a systematic path from concept to prototype. The key component in the proposed design workflow is a flexible parametric model of the helical spring, in which the lattice-based cross-section is defined by the unit cell choice (a unit cell library of 12 different cells is presented inhere), discrete and continuous variables for which the recommended ranges are identified. Heaving the parametric model in hands, a differential evolution algorithm is applied to concurrently optimize the material scale (lattice geometry) and the structural scale. From the selected library of cells, Cuboctahedron (CO) UC leads to superior performance. Incorporating a linear gradient in beam thickness (with a minimal beam radius of 0.5 mm and a scaling factor f of 1.6) has been shown to homogenize stress distribution across the spring cross-section. This guideline assists in mitigating stress concentrations, particularly at the inner coil.

Regarding the prototype manufacturing and post-processing adjustments, some auxiliary and temporary features were proposed to facilitate cleaning and avoid damaging the lattice structure. However, the experimental observations revealed an average beam radius reduction of approximately 25% due to cleaning processes. A corresponding design correction factor is thus recommended to adjust the nominal dimensions during the modeling phase to account for post-processing deviations.

Future work. One of the first avenues for further exploration are related to the lattice base material. To that end, the use of rubber-like polymers (e.g. TPU), could provide higher elasticity and energy storage capacity, while metal additive manufacturing (SLM) should offer superior mechanical performance for high-load applications.

Further perspective is related to spring's structural shape design. While this study focused on helical shape, other configurations (e.g., wave, barrel springs or auxetic structures) could be explored to enhance energy absorption. Additionally, while the unit cells in this study were inserted with fixed orientation into structured hexahedral meshes, their orthotropic symmetry ensured mechanical response was invariant under discrete 90° rotations. However, in future developments involving non-uniform meshing or composite unit cell assemblies, orientation effects could become relevant. This opens up a promising research direction involving anisotropic or meso-structured unit cells tailored for directional stiffness in complex loading scenarios.

Considering the manufacturing challenges further exploration should be undertaken to carefully tune process parameters to ensure dimensional accuracy and mechanical reliability. In addition to geometrical evaluation through CT imaging, future work will focus on microscopic-scale characterization of the lattice material surface. In particular, scanning electron microscopy (SEM) will be employed to assess sintering quality, porosity, and surface roughness. These features, not addressed in the present study, are relevant for understanding fatigue behavior and long-term performance of lattice-based springs under cyclic loading.

Another important avenue for future research is the modeling of nonlinear mechanical behavior. While the present study focuses on stiffness optimization in the elastic regime, experimental tests revealed a slight nonlinear response at higher displacements. This behavior

is likely due to a combination of large beam deflections and local plasticity or damage at partially sintered beam junctions. Capturing such effects would require geometric and material nonlinear modeling, and possibly transitioning to continuum-based finite element representations.

The integrated design framework combining parametric lattice-spring modeling, differential evolution-based multi-scale optimization, and practical manufacturing adjustments, proves to be a robust and scalable lightweight design strategy. This framework's versatility can be a aiming for high-performance sectors such as aerospace, automotive, and energy-absorbing systems, where reducing weight while maintaining mechanical integrity is paramount. Its versatility offers a scalable strategy that can be adapted to other critical structural components, paving the way for future research and industrial innovation.

Funding

This research did not receive any specific grant from funding agencies in the public, commercial, or not-for-profit sectors.

Conflicts of interest

The authors declare that they have no known competing financial interests or personal relationships that could have appeared to influence the work reported in this paper.

Data availability statement

The data that support the findings of this study are available from the corresponding author upon reasonable request.

Author contributions statement

- **Mathilde Serretiello:** Conceptualization, Methodology, Formal analysis, Writing of the original draft, Coding.
- **Manuel Paredes:** Supervision, Experimental validation, Data curation, Review.
- **Eduard Marenic:** Conceptualization, Methodology, Investigation, Supervision, Writing of the original draft, Review & editing.

All authors read and approved the final manuscript.

References

[1] L.J. Gibson, M.F. Ashby, Cellular Solids: Structure and Properties, Cambridge Solid State Science Series, 2nd edn. University Press (1997)

[2] T. Decker, S. Kedziora, Optimizing the thickness of functionally graded lattice structures for high-performance energy absorption: a case study based on a bicycle helmet, Appl. Sci. **14**, 2788 (2024)

[3] S.K. Moon, Y.E. Tan, J. Hwang, Y.J. Yoon, Application of 3D printing technology for designing light-weight unmanned aerial vehicle wing structures, Int. J. Precis. Eng. Manuf. Green Technol. **1**, 223–228 (2014)

[4] N. Khan, A. Riccio, A systematic review of design for additive manufacturing of aerospace lattice structures: current trends and future directions, Progr. Aerospace Sci. **149**, 101021 (2024)

[5] E. Sacco, Analysis and Modelling of 3D Printed Springs for Use in Spacecraft, PhD Thesis, Nanyang Technological University (2020)

[6] J. Souza, A. Grossmann, C. Mittelstedt, Micromechanical analysis of the effective properties of lattice structures in additive manufacturing, Additive Manuf. **23**, 53–69 (2018)

[7] Y. Wu, J. Fang, C. Wu, C. Li, G. Sun, Q. Li, Additively manufactured materials and structures: a state-of-the-art review on their mechanical characteristics and energy absorption, Int. J. Mech. Sci. **246**, 108102 (2023)

[8] G. Cadet, M. Paredes, Enhanced design parameters of a cylindrical helical compression spring using an optimization algorithm and a non-linear behavior model, Mech. Based Des. Struct. Mach. **52**, 9609–9620 (2024)

[9] M. Paredes, Analytical and experimental study of conical telescoping springs with nonconstant pitch, J. Mech. Des. **135**, 094502 (2013)

[10] Z. Wu, M. Paredes, S. Seguy, Targeted energy transfer in a vibro-impact cubic nes: description of regimes and optimal design, J. Sound Vibr. **545**, 117425 (2023)

[11] Y. Li, M. Li, Y. Liu, X. Geng, C. Cui, Parameter optimization for torsion spring of deployable solar array system with multiple clearance joints considering rigid-flexible coupling dynamics, Chinese J. Aeronaut. **35**, 509–524 (2022)

[12] H. Lei, C. Li, J. Meng, H. Zhou, Y. Liu, X. Zhang, P. Wang, D. Fang, Evaluation of compressive properties of SLM-fabricated multi-layer lattice structures by experimental test and μ-CT-based finite element analysis, Mater. Des. **169**, 107685 (2019)

[13] L. Liu, P. Kamm, F. García-Moreno, J. Banhart, D. Pasini, Elastic and failure response of imperfect three-dimensional metallic lattices: the role of geometric defects induced by selective laser melting, J. Mech. Phys. Solids **107**, 160–184 (2017)

[14] M. Saleh, A.E. Ragab, Ti-6Al-4V helical spring manufacturing via SLM: effect of geometry on shear modulus, Proceedings of the International MultiConference of Engineers and Computer Scientists, Vol. **2**, Hong Kong, IMECS (2013)

[15] M.R.U. Haq, A. Nazir, J.Y. Jeng, Design for additive manufacturing of variable dimension wave springs analyzed using experimental and finite element methods, Additive Manuf. **44**, 102032 (2021)

[16] L. He, H. Peng, M. Lin, R. Konjeti, F. Guimbretière, J.E. Froehlich, Ondulé, Designing and controlling 3D printable springs, Proceedings of the 32nd Annual ACM Symposium on User Interface Software and Technology, 739–750 (2019)

[17] Y.M. Hailu, A. Nazir, S.C. Lin, J.W. Jeng, The effect of functional gradient material distribution and patterning on torsional properties of lattice structures manufactured using multijet fusion technology, Materials **14**, 6521 (2021)

[18] nTop Inc., nTop Documentation, Implicit and Other Models, https://ntop.com

[19] G. Cadet, M. Paredes, A new exhaustive semi-analytical method to calculate stress distribution on the surface of a curved beam with circular cross section, with an application to helical compression springs, Eur. J. Mech. A: Solids **103**, 105191 (2024)

[20] G. Cadet, M. Paredes, H. Orcière, Improved analytical model for cylindrical compression springs not ground considering end behavior of end coils, Mech. Ind. **22**, 50 (2021)

[21] P. Virtanen, R. Gommers, T.E. Oliphant, M. Haberland, T. Reddy, D. Cournapeau, E. Burovski, P. Peterson, W. Weckesser, J. Bright, S.J. van der Walt, M. Brett, J. Wilson, K.J. Millman, N. Mayorov, A.R.J. Nelson, E. Jones, R. Kern, E. Larson, C.J. Carey, İ. Polat, Y. Feng, E.W. Moore, J. VanderPlas, D. Laxalde, J. Perktold, R. Cimrman, I. Henriksen, E.A. Quintero, C.R. Harris, A.M. Archibald, A.H. Ribeiro, F. Pedregosa, P. van Mulbregt, SciPy 1.0 contributors, SciPy 1.0: fundamental algorithms for scientific computing in Python, Nat. Methods **17**, 261–272 (2020)

[22] J. Noronha, J. Dash, M. Leary, M. Watson, M. Qian, E. Kyriakou, M. Brandt, Additively manufactured functionally graded lattices: design, mechanical response, deformation behavior, applications, and insights, JOM **75**, 5729–5754 (2023)

[23] C. Top, Ö. Sahin, H.S. Gökçe, Mechanical properties of functionally graded lattice structures derived using computer-aided design for additive manufacturing, Appl. Sci. **13**, 11667 (2023)

[24] N. Lammens, M. Kersemans, I. De Baere, W. Van Paepegem, On the visco-elasto-plastic response of additively manufactured polyamide-12 (PA-12) through selective laser sintering, Polym. Test. **57**, 149–155 (2017)

[25] R. Rodríguez-Aparicio, J.M. Alegre, W.M.H. Verbeeten, M. Lorenzo-Bañuelos, I.I. Cuesta, Methodology to predict mechanical properties of PA-12 lattice structures manufactured by powder bed fusion, Additive Manuf. **78**, 103864 (2023)

[26] L. Liu, Elastic and failure response of imperfect three-dimensional metallic lattices: the role of geometric defects induced by selective laser melting, J. Mech. Phys. Solids **25**, 160–184 (2017)

Cite this article as: M. Serretiello, M. Paredes, E. Marenic, Numerical and experimental modelling of mechanical springs made of lattice material, Mechanics & Industry **26**, 33 (2025), https://doi.org/10.1051/meca/2025026